Bulletin of Volcanology (2018) 80: 29
https://doi.org/10.1007/s00445-018-1192-6

RESEARCH ARTICLE

UAV-based remote sensing surveys of lava flow fields: a case study from Etna's 1974 channel-fed lava flows

Massimiliano Favalli[1] · Alessandro Fornaciai[1,2] · Luca Nannipieri[1] · Andrew Harris[3] · Sonia Calvari[4] · Charline Lormand[5]

Received: 31 July 2017 / Accepted: 4 January 2018 / Published online: 26 February 2018

Abstract

During an eruption, time scales of topographic change are fast and involve vertical and planimetric evolution of millimeters to meters as the event progresses. Repeat production of high spatial resolution terrain models of lava flow fields over time scales of a few hours is thus a high-value capability in tracking the buildup of the deposit. Among the wide range of terrestrial and aerial methods available to collect such topographic data, the use of an unmanned aerial vehicle (UAV) as an acquisition platform, together with structure from motion (SfM) photogrammetry, has become especially useful. This approach allows high-frequency production of centimeter-scale terrain models over kilometer-scale areas, including dangerous and inaccessible zones, with low cost and minimal hazard to personnel. This study presents the application of such an integrated UAV-SfM method to generate a high spatial resolution digital terrain model and orthomosaic of Mount Etna's January–February 1974 lava flow field. The SfM method, applied to images acquired using a UAV platform, enabled the extraction of a very high spatial resolution (20 cm) digital elevation model and the generation of a 3-cm orthomosaic covering an area of 1.35 km^2. This spatial resolution enabled us to analyze the morphology of sub-meter-scale features, such as folds, blocks, and cracks, over kilometer-scale areas. The 3-cm orthomosaic allowed us to further push the analysis to centimeter-scale grain size distribution of the lava surface. Using these data, we define three types of crust structure and relate them to positions within a channel-fed a ā flow system. These crust structures are (i) flow parallel shear lines, (ii) raft zones, and (iii) folded zones. Flow parallel shear lines are found at the channel edges, and are 2-m-wide and 0.25-m-deep zones running along the levee base and in which cracking is intense. They result from intense shearing between the moving channel lava and the static levee lava. In zones where initial levees are just beginning to form, these subtle features are the only marker that delimits the moving lava from the stagnant marginal lava. Rafts generally form as the system changes from a stable to a transitional channel regime. Over this 170-m-long zone, the channel broadens from 8 to 70 m and rafts are characterized by topographically higher and poorly cracked areas, surrounded by lower, heavily cracked areas. We interpret the rafts as forming due to breakup of crust zones, previously moving in a coherent manner in the narrow proximal channel reach. Folded zones involve arcuate, cross-flow ridges with their apexes pointing down-flow, where ridges have relatively small clasts and depressions are of coarser-grained breccia. Our folds have wavelengths of 10 m and amplitudes of 1 m; are found towards the flow front, down-flow of the raft zones; and are associated with piling up of lava behind a static or slowly moving flow front. The very high spatial resolution topographic data available from UAV-SfM allow us to resolve surfaces where roughness has a vertical and horizontal scale of variation that is less than 1 m. This is the case over pāhoehoe and a ā flow surfaces, and

Editorial responsibility: M.R. James; Deputy Executive Editor: J. Tadeucci

Electronic supplementary material The online version of this article (https://doi.org/10.1007/s00445-018-1192-6) contains supplementary material, which is available to authorized users.

✉ Alessandro Fornaciai
alessandro.fornaciai@ingv.it

[1] Istituto Nazionale di Geofisica e Vulcanologia, via della Faggiola 32, 56126 Pisa, Italy

[2] Dipartimento di Fisica, Settore di Geofisica, University "Alma Mater Studiorum", Viale Carlo Berti Pichat 8, 40127 Bologna, Italy

[3] CNRS, IRD, OPGC, Laboratoire Magmas et Volcans, Université Clermont Auvergne, F-63000 Clermont-Ferrand, France

[4] Istituto Nazionale di Geofisica e Vulcanologia – Osservatorio Etneo, Piazza Roma 2, 95125 Catania, Italy

[5] Volcanic Risk Solutions, Institute of Agriculture and Environment, Massey University, Private Bag 11 222, Palmerston North 4442, New Zealand

thus allows us to explore those new structures that are only apparent in the sub-metric data. Moreover, during future eruptions, the possibility to acquire such information in near-real time will allow a prompt analysis of developing lava flow fields and structures therein, such as developing lava channel systems, so as to contribute to timely hazard assessment, modeling, and projections.

Keywords Unmanned aerial vehicle (UAV) · Structure from motion (SfM) · Digital elevation model (DEM) · Etna 1974 eruption · Lava flow

Introduction

Lava flow morphometric analysis is essential for defining lava flow systems and their associated flow dynamics (e.g., Lipman and Banks 1987; Rossi 1997; Lev and James 2014; Dietterich and Cashman 2014; Dietterich et al. 2015). In quantifying lava flow field morphologies, generation of digital elevation models (DEMs) and acquisition of visible and thermal imagery are necessary first steps (e.g., Mazzarini et al. 2005; James et al. 2009; Tarquini et al. 2012). These tasks have traditionally been the role of remote sensing, where sensors operating at the appropriate wavebands, and flown on satellite and airborne platforms, offer an efficient means of achieving full spatial coverage of extensive, remote and/or inaccessible, lava flow fields (Francis and Rothery 2000). Building on well-developed photogrammetric methods (e.g., Lillesand et al.1987), efforts in the 1990s focused on use of "high" spatial resolution (10 m pixel) data from satellite-based sensors, such as SPOT, coupled with ground-based electronic distance measurement surveys to furnish lava flow field DEMs with spatial resolutions of around 10 m (Stevens et al. 1999). Ground-based GPS surveys, coupled with use of laser-range finder total stations allowed spatial resolutions of order 1 m, but data collection was time consuming and only possible for small areas within the flow field system (James et al. 2009; Harris et al. 2009). Instead, airborne LiDAR imaging offered a 1-m capability for entire channel-fed systems (Mazzarini et al. 2005; Favalli et al. 2010a, b) and lava flow fields (Favalli et al. 2009; Behncke et al. 2016), but mission deployment was costly, and acquisition of high point densities over poorly reflective, basaltic surfaces limited the spatial resolution and number of points available per pixel (Fornaciai et al. 2010; Kolzenburg et al. 2016). Tripod-mounted LiDAR systems coupled with thermal camera imaging have allowed sub-metric spatial resolution, as well as temporal resolutions of a few minutes (James et al. 2009; Slatcher et al. 2015). But again, coverage is limited and highly oblique viewing conditions can introduce extensive shadow zones (Richter et al. 2016).

In the last few years, the structure-from-motion (SfM) computer vision technique has provided a low-cost and user-friendly tool for generating high spatial resolution digital topography using images acquired by consumer-grade digital camera images. The SfM method solves for camera position and scene geometry simultaneously and automatically, using a highly redundant bundle adjustment based on matching features in multiple overlapping images (Favalli et al. 2012; James and Robson 2012; Westoby et al. 2012; Nouwakpo et al. 2016). The SfM method and the improvements in quality of consumer-grade digital cameras and methods for camera calibration have thus encouraged the use of digital photogrammetric techniques for 3D modeling of volcanic features over recent years (James and Varley 2012; Tuffen et al. 2013; James and Robson 2014a; Farquharson et al. 2015; Kolzenburg et al. 2016; Richter et al. 2016; Neri et al. 2017).

In parallel with SfM methods, proliferation of unmanned aerial vehicles (UAVs), often known as "drones," has presented a new, flexible, low-cost platform option for the acquisition of images. UAVs represent an excellent platform to make the best use of the SfM method. Capable of overflying large areas in a short period of time and of operating below cloud decks that block satellite views, the flexibility of operation, the possibility of high temporal resolution and spatial resolutions, as well as the array of cheap sensor payload options make a UAV-mounted camera system an outstanding new option for the volcano remote sensor. The centimetric spatial scale and high temporal resolutions possible from the UAV-based perspective allow extension and combination of existing methodologies and development of new methodologies to allow a fully integrated analysis of volcanic topographies, structures, and processes at a variety of spatial scales. The result is a significant advance in our power to analyze, track, and understand dynamic Earth surface morphologies, allowing improved monitoring, surveillance, and science.

We here review and further develop an integrated methodology that combines UAV-based remote sensing with the SfM method through application to a morphometric analysis of a channel-fed lava flow field. UAV-SfM methodologies are now quite well-developed in other disciplines (e.g., Mancini et al. 2013; Lucieer et al. 2014), and are beginning to be applied also in volcanology (Nakano et al. 2014; Perroy et al. 2015; Fornaciai et al. 2017; Müller et al. 2017).

Background

In 2005, we completed an airborne LiDAR campaign on Etna, which allowed construction of a 1-m spatial resolution DEM covering most of the edifice (Favalli et al. 2009). One-meter-pixel LiDAR data have already allowed us to complete

morphological analyses of lava channels (Mazzarini et al. 2005) and channel-fed systems (Favalli et al. 2010a) and to carry out best-fit modeling of lava flow down channelized systems (Harris et al. 2007). As described by Cashman et al. (2013), other relevant lava flow features that can be mapped to aid in interpretation of lava flow emplacement dynamics are surface folds, tumuli, fractures, blocks, and lobate flow fronts. In particular, lava surface folding involves surface-parallel shortening, and will not occur unless the viscosity of the fluid decreases with depth (Gregg and Fink 2000; Lescinsky and Merle 2005). Surface folds are common on lava flows of all compositions, and they range in amplitude (A) and wavelength (λ) from centimeters (in pāhoehoe flows) to tens or hundred meters (in obsidian flows). Wavelengths of folding depend primarily on the compressive stresses, temperature profile of the flow, and the viscosity and density of the lava (Fink and Fletcher 1978; Fink 1980). However, folds, tumuli, fractures, blocks, and lobate flow fronts often have sub-meter spatial scales and are thus difficult to resolve in the 1-m Etna LiDAR DEM. Generally speaking, for surfaces where roughness has a vertical and horizontal scale of variation that is less than 1 m, which is the case over pāhoehoe and a ā flows (e.g., Crown and Baloga 1999), 1-m DEMs are not capable of imaging the whole spectrum of variation.

We thus, here, generate a very high spatial resolution (20 cm) DEM, as well as a 3-cm spatial resolution orthomosaic, for the entire lava flow field of Etna's 1974 eruption, containing three well-developed lava channels (Fig. 1), through UAV-SfM. To do this, we use photos collected with a consumer-grade camera during UAV-based over flights in May and September 2015. The SfM-derived DEM is compared with the 1-m LiDAR-derived DEM, where we qualitatively and quantitatively describe the advantages of increasing the DEM resolution up to the decimeter scale when completing morphometric analyses. Qualitative analysis is carried out using our 20-cm resolution DEM to define those new structures apparent in the sub-metric data. Quantitative analysis is carried out by comparing the S-transform of selected profiles calculated over the two DEMs at different resolutions in order to detect different local structures and patterns. Finally, the very high spatial resolution topography of Etna's 1974 lava flow field was used to measure morphometric parameters through extraction of profiles normal to the flow direction from the DEM (Mazzarini et al. 2005; Tarquini et al. 2012; Deardorff and Cashman 2012; Chevrel et al. 2013; Dietterich and Cashman 2014). This was completed for three lava channels which represented different stages of channel evolution: a mature channel, an immature channel with low yield strength, and an immature channel with high yield strength, allowing their component structures, and their extension and development in space and time, to be defined.

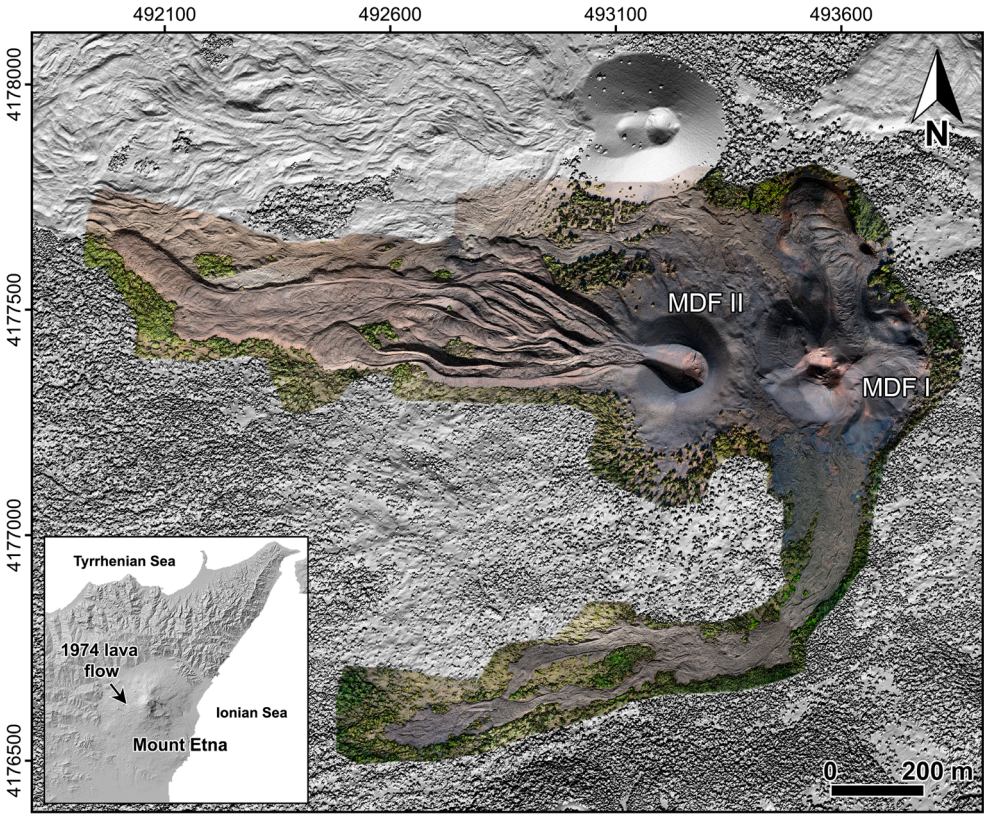

Fig. 1 UAV-data-derived orthophoto mosaic of Mt. Etna's 1974 lava flow and cone system overlaid on the shaded relief derived from a merge of the 1-m and 20-cm DEMs. The RGB area indicates the area imaged during the UAV surveys and where the DEM was reconstructed starting from the photos. MDF I and MDF II stand for Mount De Fiore I and II, respectively. The inset shows the location of the 1974 lava flow on Mount Etna

The 1974 Mount Etna flank eruption

The 1974 eruption of Mount Etna occurred at a relatively low elevation (~ 1660 m a.s.l.) on the west flank, a location approximately 6 km from the summit craters and 6 km from the nearest villages (Fig. 1). It consisted of two phases of activity separated by 22 days of quiescence (Bottari et al. 1975). Effusive and explosive activity built up two compound lava flow fields and two scoria cones, named the Monte De Fiore I and II (Fig. 1). The first eruptive phase began on 30 January and produced the cinder cone of Monte De Fiore I (MDF I), which reached a height of about 70 m and a width of 300 m in just a few days (Corsaro et al. 2009). The first phase involved ten discrete lava fountaining and effusive episodes that produced ten individual lava flow units (Tanguy and Kieffer 1977), and stopped on 16 February. A new, highly explosive activity began on 11 March and rapidly built the 50-m-high cinder cone of Monte De Fiore II (MDF II), from which lava flows advanced westward. The eruption ended on 29 March.

Materials and methods

Acquisition system

Photogrammetric campaigns were carried out using a Dà-Jiāng Innovations Science and Technology Co. Ltd. (DJI) hexacopter (model F550), with an onboard GPS system and internal gyroscope (Fig. 2). The hexacopter has a payload capacity of around 2.4 kg. The 10,900-mAh battery provides about 20 min of flight time. The Ground Station Software v4.0.11 allows the flight plan (including platform velocity, altitude, and direction) to be defined and uploaded to the onboard autopilot. The autopilot also ensures platform stability by controlling the craft pitch, roll, and yaw using the real-time information feed from the gyroscope. There is also an option of radio control, which includes a return-direct-to-base (mission abort) button. Further details about the UAV system used in this work are described in Nannipieri et al. (2016). Italian flight operations law requires two independent radio control systems to be deployed so that a backup is always on site. The second system cuts power to the drone if contact with the first system is lost, thereby terminating the flight. The UAV was equipped with a consumer-grade Sony NEX-5T, a 16-megapixel camera which is 111 mm × 59 mm × 38 mm in size, weighs 0.39 kg, and can provide 4912 × 3264 pixel images. The E 16–50-mm zoom lens has a 24–75-mm focal length, an 83–32° field of view, and a minimum aperture of f/22–f/36. Camera calibration was completed by using the lens tool function of PhotoScan Pro 1.2, which uses a standard black-and-white chessboard grid to calculate the lens focal length and distortion properties so as to provide a lens-distortion correction.

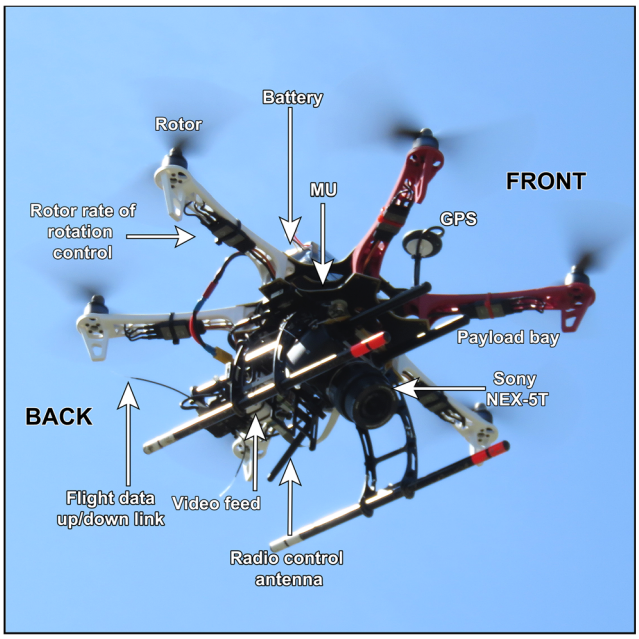

Fig. 2 The platform and sensor system used during the survey. MU stands for management unit

UAV field survey of the 1974 lava flow

Flight planning needs to be set up so as to ensure a flight altitude, craft velocity, and imaging frequency that provide sufficient overlap between images to allow SfM reconstruction. All acquisitions were at a fixed zoom of 16 mm, and images were acquired at an oblique angle of 24° from vertical. As a result, pixel viewing angles range from 0° (for the pixel immediately below the drone) to 48° at the image edge. This ensures that each pixel is viewed at sufficiently diverse angles so as to reduce overall geometric errors when compared with a vertical view (James and Robson 2014b). If we set flight altitude to 70 m above-ground level (AGL), for an angular field of view of 83°, the image area will be trapezoidal with a width of 78 m and a length of 104 m for its short edge and 157 m for its long edge, giving an image area of 10,179 m^2. This gives a nominal pixel size of 2.5 cm. If we image once every two seconds at a craft velocity of 10 m/s, we will thus image every 20 m of flight, meaning that each point is imaged in the flight path direction four times from four different angles. Given overlapping flight paths in the cross-track direction, each point is imaged up to 21 times. This flight plan was entered into the Ground Station Software v4.0.11. The result is displayed on Google Earth™ for checking, and the flight plan can then be uploaded to the autopilot. Flight time is taken into account when setting up the flight plan and cannot exceed the battery lifetime of 20 min. Flight planning also needs to take into account national flight law. For the 1974 lava survey, we needed to follow the regulations of ENAC (Ente Nazionale per l'Aviazione Civile) that covers UAV (SAPR—Sistema Aeromobile a Pilotaggio Remoto—in Italian) operations over

Italian sovereign airspace. At the same time, the camera is programmed to image once every two seconds, with images stored in raw format on the camera internal memory card. Raw image size is 48 Mb, so for 12 min of acquisition at a 2-s frame rate, card capacity needs to be 28.8 Gb. This capacity can be reduced to around 5 Gb if images are collected in JPEG format, but use of the JPEG format reduces the final accuracy of the model (Agisoft Photoscan 2013). We carried out 11 flights (Fig. 3) during two different campaigns, acquiring 2781 photographs over a total flight distance of about 40 km, which was completed during a total flight time of 124 min. From this, we built six topographic models, which covered six overlapping areas across the target zone. These, when merged, provided complete coverage of the lava flow field (Fig. 3).

DEM and orthomosaic generation

SfM DEM generation

The 3D model was generated using SfM as implemented by Agisoft PhotoScan Professional version 1.2. As a preliminary step, we organized the acquired photos into six different photo sets. This was necessary because the data set was particularly large and because the photographs were collected on different days and/or under variable lighting conditions. To build the 3D model, we input the images and camera calibration parameters into PhotoScan Pro 1.2. The automated image feature identification routine was run to find corresponding features in different images using an algorithm able to correctly detect the same features over a large image dataset, regardless of the changes in orientation, scale, illumination, or 3D position. In step 2, by matching features identified in multiple images, the camera positions were resolved and scene geometry obtained by applying a highly redundant bundle adjustment. This output an initial, sparse, point cloud. Step 3 thus involved creation of a dense cloud, which was derived directly using the, now known, camera position relative to each image. This step is termed multiview stereo matching (MSV). This workflow allowed derivation of 270×10^6 points, from the 2781 photographs input, over a total area of 1.35 km^2, for a point density of 200 points per square meter (Fig. 4a).

The point clouds generated by Photoscan must be now positioned, oriented, and scaled. To do this, first, three points at different spatial positions in the cloud were identified using Scanalyze software and tied to ground control points using a simple C++ code to allow initial, approximate, georeferencing of the slave (the point cloud) to the master, which in this case was the 2005 LiDAR-derived DEM of Mount Etna as generated by Favalli et al. (2009). To more precisely match the point cloud to the surface, we minimized the root mean square (RMS) error between the master (reference LiDAR DEM) and the slave (the SfM point cloud) by iteratively varying the three angles of rotation, the translation, and the magnification or

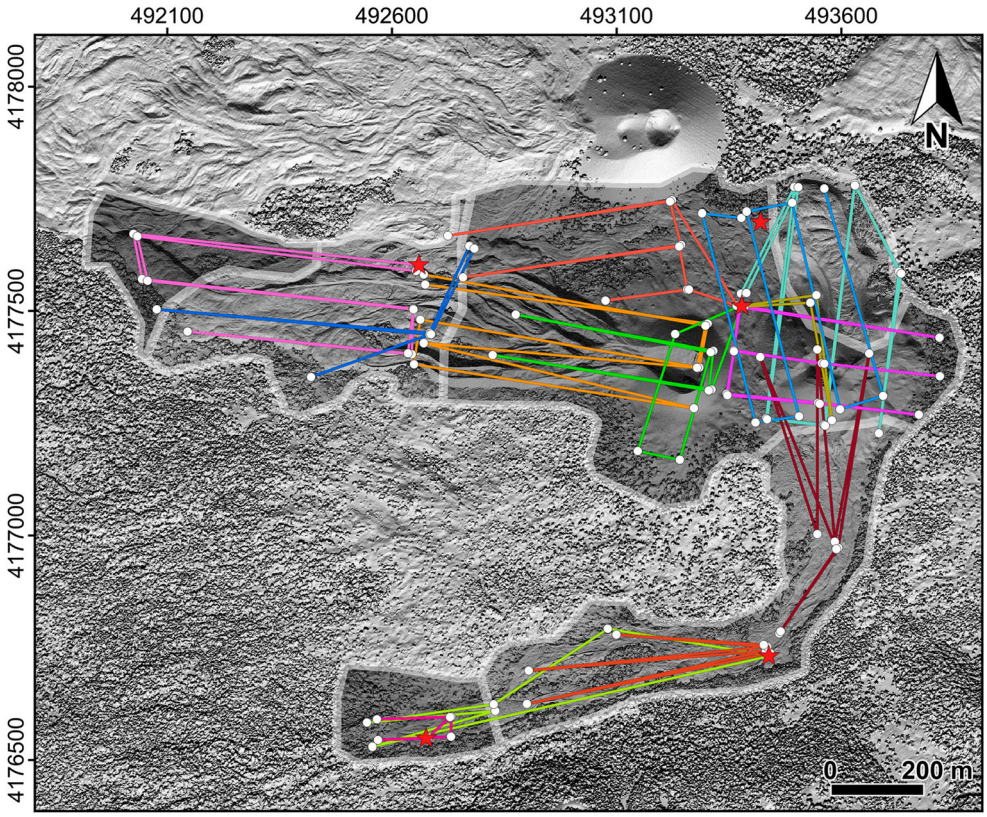

Fig. 3 Flight plan for the survey of the 1974 lava flow field with the six sub-areas imaged during each flight. Solid lines mark UAV flight paths, dots give each change in flight direction, and stars are the launch/landing locations

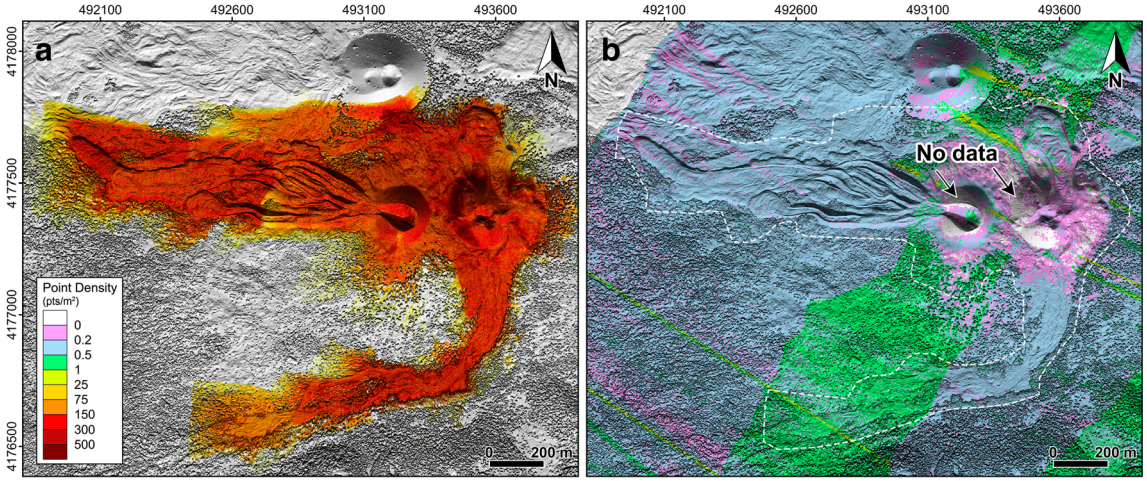

Fig. 4 Point density distributions of the SfM and LiDAR 3D models. **a** Point density distribution of the 1974 lava flow reconstructed using UAV-SfM methods. **b** LiDAR point density distribution over the investigated area (see **a** for legend). The dotted line indicates the area reconstructed using the UAV-Sony NEX-5T system

reduction factor of the slave using a custom-made algorithm based on the MINUIT minimization library (James and Roos 1977), as described by Kolzenburg et al. (2016) and Richter et al. (2016). MINUIT is a tool to find the minimum value of multiparameter functions and can be freely downloaded (http://www.cern.ch/minuit). Our RMS error is the root mean square residuals (in elevation) between the SfM point cloud and the reference LiDAR DEM, rather than a true absolute error. Best fit was obtained with an RMS error of 0.24 m.

Six DEMs (Fig. 3) were created from the six georeferenced point clouds. Given the point density, we could quantize the data into a 20-cm pixel grid, meaning that we had eight points per pixel on average. These six DEMs were merged to create a single very high spatial resolution DEM of the 1974 lava flow field, which is provided here as a GEOTIFF file (see supplementary material). The orthomosaic (Figs. 1 and 5) was then created automatically using the build orthomosaic tool of PhotoScan Pro. In setting up this tool, we were careful to maintain the spatial resolution of the original images by entering 3 cm at the output resolution prompt. PhotoScan Pro then orthorectified each pixel and built the orthomosaic. The output image was 66,000 × 44,000 pixels, or almost 9 Gb in size as RGB image, and covered a ground area of 1.98 × 1.32 km. Finally, the 3-cm resolution orthomosaic was georeferenced to the 20-cm DEM. The orthomosaic of 1974 Etna lava flow resampled to 20 cm is provided here as an RGB GEOTIFF image (see supplementary material).

DEM accuracy

Elevations for each pixel in our DEM are the mean value for all points within the pixel. Thus, to describe variability inside each pixel, we used the standard deviation (σ) for each pixel. Generally, variability within a pixel was 1–3 cm, being highest over vegetated zones (especially trees) where σ was greater than 1 m, depending on the height of the bush or tree (Fig. 6). We also found linear artifacts, in correspondence to pixels in which we had a high (10–15) number of points, around the projected edges of a few photos, in which the end of a leg of the drone had been imaged. To clean up these artifacts, we rejected all points that were greater than 2σ from the mean and recalculated the pixel mean value. To understand the difference between the two DEMs, we resampled the UAV-derived DEM to 1 m, so as to make it comparable with the spatial resolution of the LiDAR DEM. The RMS difference, across zones where we had both LiDAR and UAV coverage and excluding vegetated regions, was 0.22 m.

DEM-derivative maps

Using the 1-m LiDAR DEM of the 1974 lava flow field and the 20-cm UAV-derived DEM, we next derived parameters that can be useful for lava flow morphometric analysis (Favalli and Fornaciai 2017), that is, shaded-relief, sky view factor (SVF), and openness down maps (Fig. 7). These were obtained from the 20-cm DEM placed into the LiDAR DEM. Placement of the former into the latter is merely esthetically pleasing, allowing a rectangular region of analysis and map to be set up. To complete this merge, each 1-m LiDAR DEM pixel was divided into twenty-five 20-cm pixels across which values were interpolated. These values were used to fill the empty areas of the rectangular grid, especially around the irregular area defined by the limit of drone coverage (Fig. 3).

The sky view factor was described by a solid angle (Ω) open to the sky and expressed in terms of the total sky view

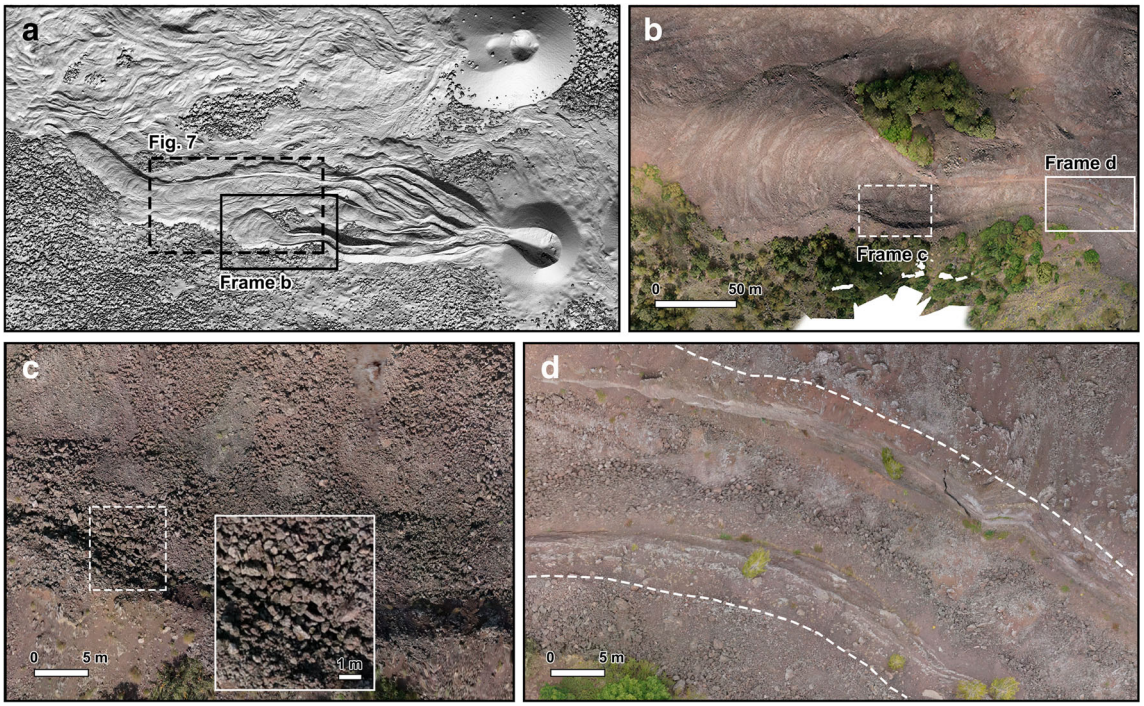

Fig. 5 Region of interest extracted from the 3-cm orthomosaic image showing the centimeter-scale grain distribution of the lava surface at different scales. **a** Location of frame b. **b** Lava channel and dispersed flow with the location of frames c and d. **c** Lava channel near the transition zone. The presence of meter-sized blocks, especially at the base of the levee inner flank, is evident. **d** Section of lava channel taken from the othomosaic. Differences in grain size across the levee (dashed lines give the outer levee base), as well as across the channel, are evident

possible from any given pixel, i.e., SVF = $\Omega/2\pi$ (Favalli and Fornaciai 2017). It is thus the fraction of the sky visible from each pixel and ranges from one to zero and was calculated following Zakšek et al. (2011). To speed up the process,

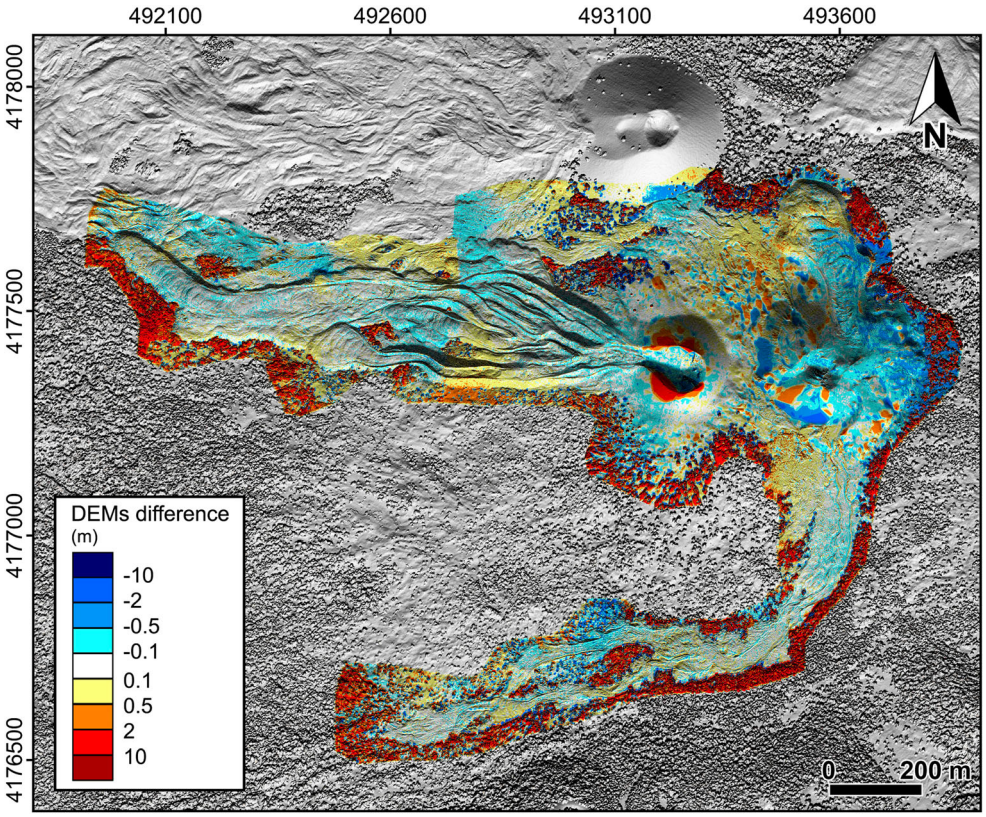

Fig. 6 SfM and LiDAR DEM difference to quantify the displacement (and distribution of displacement) between the two DEMs

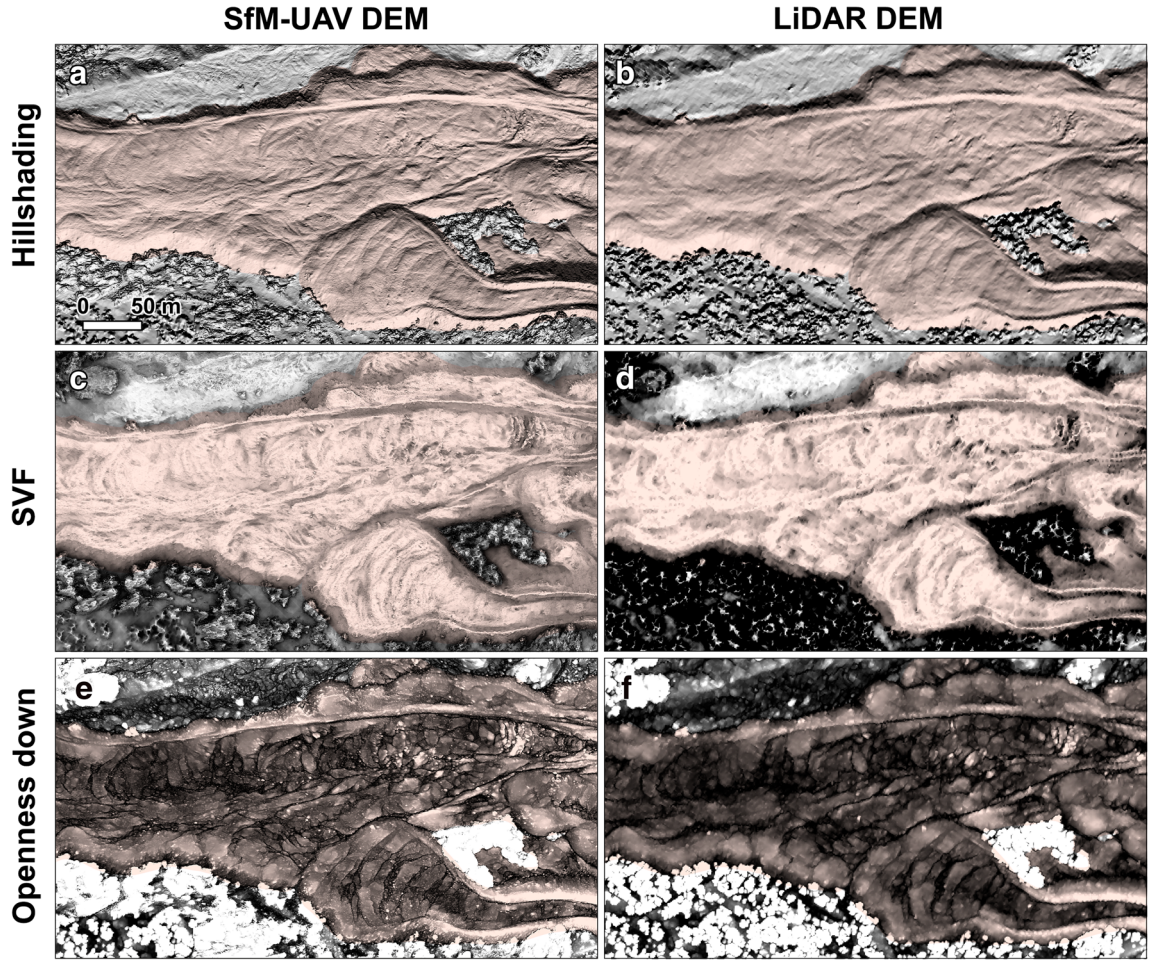

Fig. 7 SfM-UAV and LiDAR DEM comparison of a region of interest (ROI). Location of ROI is given in Fig. 5. **a** Hill-shaded map, **c** sky view, and **e** openness down (crack map) image derived from the 20-cm DEM; **b** hill-shaded map, **d** sky view, and **f** openness down (crack map) derived from the 1-m DEM

SVF is usually calculated by considering the openness to the sky along a number of directions (n), instead of calculating it at each point of a DEM (Zakšek et al. 2011; Favalli and Fornaciai 2017) using the equation

$$\mathrm{SVF} = 1 - \frac{1}{n}\sum_{i=1}^{n} \sin\gamma_i$$

where γ_i is the elevation angle of the visible horizon along a given direction. Ridges will be incident to nearly all of the incoming light, and so will have values close to one. For depressions, the opposite will hold. Thus, this method is extremely effective in mapping ridges, which in our case include levee rims (Fig. 7c, d). Yokoyama et al. (2002) introduced two parameters termed positive (Φ_R) and negative openness (Ψ_R) (hereafter labeled openness up and openness down, respectively) defined as

$$\Phi_R = 90^\circ - \frac{1}{n}\sum_{i=1}^{n} \gamma_i \quad \text{and} \quad \Psi_R = 90^\circ - \frac{1}{n}\sum_{i=1}^{n} \psi_i$$

where the subscript R refers to the maximum horizontal search radius considered, γ_i is defined as above, and ψ_i is the angle of visible horizon from a given point i towards the ground (Favalli and Fornaciai 2017). While Φ_R is a measure of the openness of the terrain to the sky, Ψ_R is the below-ground openness (Yokoyama et al. 2002; Karátson et al. 2016; Favalli and Fornaciai 2017). Openness up has high values at crests and ridges, and it is similar to the SVF, but openness down has high values inside valleys, gullies, and craters. Because narrow cracks and fractures will form sharp incisions, they will have high openness down values (Fig. 7e, f). Thus, the openness down map is extremely effective in locating highly fractured areas of the lava flow surface, so much so that we termed the resultant product a crack map.

Results and discussion

Interpretation of lava flow crust and fold systems

In Fig. 7, we compare the distal section of an a ā flow system using the 20 cm and 1 m data. Because the spatial scale of

roughness is less than 1 m, only in the 20-cm derived products can we acquire a sense of roughness and map the microstructure of the flow surface. The texture of the 20-cm openness down map (Figs. 7e and 8) in particular reveals three classes of roughness: relatively smooth, rough, and mixed. These classes are defined by differences in the clast sizes that make up the a ā surface, where clasts of the smooth group are relatively small and those of the rough class are relatively large. The mixed class contains a range of clast sizes with scattered large blocks. These large blocks are probably rafted levee boats (Lipman and Banks 1987), or levee blocks that have collapsed onto the flow surface once the channel became inactive (Harris et al. 2009). Next, we see that the detail of the surface structure allows the fractal form of folds, which involve folding scales from a few meters to tens of meters, to be resolved. For example, the frontal fold in the image of Figs. 7 and 8 is about 20 m wide. However, cross-flow, this develops into a double-fold system, within which each fold is 10 m wide. At the right bank, we have at least four components to the fold, as revealed only in the 20-cm openness down map. The 20-cm SVF map (Fig. 7c) reveals that the crests of the folds are rougher than the troughs. Reference to the 20-cm shaded relief confirms that fold crests are dominated by finer-grained material than the troughs, the troughs being blockier (Fig. 7a).

Surface structures: a tripartite classification and flow regime association

The combination of a 3-cm resolution orthophoto and a 20-cm resolution DEM allows us to define three types of surface structure and relate them to positions within a channel-fed a ā flow system. These crust structures are (i) flow parallel shear lines, (ii) raft zones, and (iii) folded zones (Figs. 5 and 8). Each are associated with different spatial distributions of cracking, roughness, and clast size, and characterize different flow regimes.

Flow parallel shear lines are found at the channel edges. These structures are long, narrow continuous depressions in which cracking is intense and clast sizes are intermediate between the small clasts of the levee wall and the larger clasts of the channel (Figs. 5d and 8). Where levees are well formed and distinct, these shear lines run along the base of the levee inner wall and are typically less than 2 m wide and 0.25 m deep. Given their location, they must result from intense shearing between the moving channel lava and the static levee lava. In zones where initial levees are just beginning to form, these subtle features are the only geomorphological marker that delimits the moving lava from the stagnant marginal lava. As Lipman and Banks (1987) pointed out, across this distal "transitional" channel zone, the channel-levee boundary can be indistinct because the channel is, in effect, brim full and the levees have no positive expression. These linear features are thus extremely useful in delimiting the channel in the distal reach of the flow system, where their topographic subtleness means that it is generally the crack map that identifies these structures distally.

Rafts generally form as the system changes from a stable to a transitional channel regime. Over this zone, the channel broadens significantly. In our case, the channel broadens over a distance of 170 m, from 8 m at the exit of the stable channel to 70 m in the transitional channel. Rafts are only apparent in the openness down map (Fig. 7e), being characterized by topographically higher and poorly cracked areas, surrounded by lower, heavily cracked areas. Dimensions are up to 10 m, and raft distributions resemble patterns created by pāhoehoe slab breakup (e.g., Guest

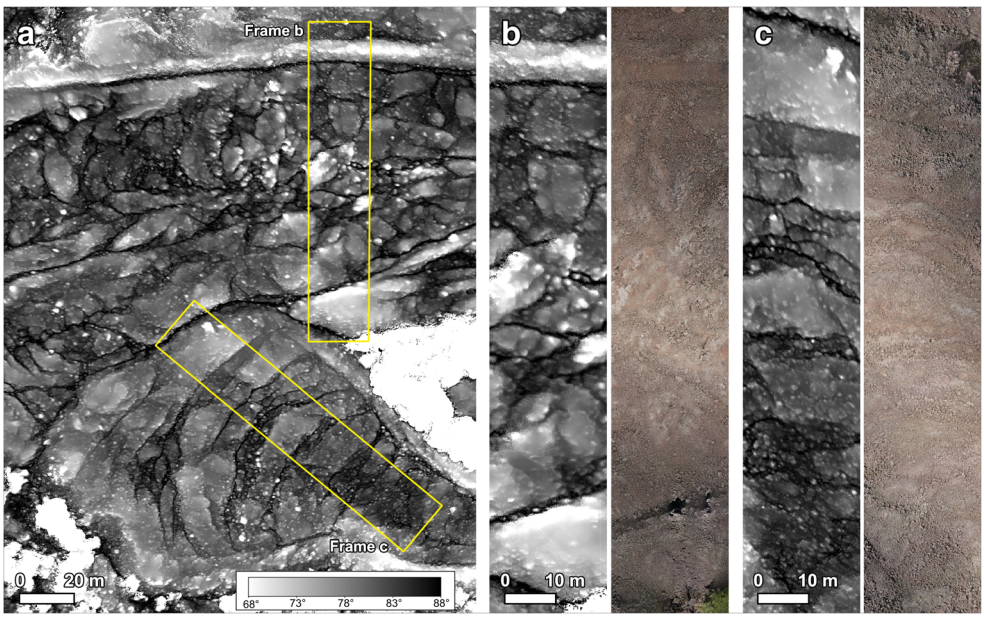

Fig. 8 Openness down map for a zone of dispersed flow and stable channel contained lava derived from the SfM-UAV DEM. **a** Overview of the selected area; **b** openness down map (left) and orthomosaic (right); **c** openness map (left) and orthomosaic (right) magnification of the zone of dispersed flow

and Stofan 2005). Close to the levee, the long axes of rafts are orientated down-flow but, towards the channel-center, orientations are random. We interpret these rafts as being formed by breakup of crust zones, previously moving in a coherent manner in the narrow proximal channel reach, as the flow exits the stable channel and enters a wider channel reach.

Folded zones involve arcuate, cross-flow pressure ridges with their apexes pointing down-flow (Fink 1980; Lipman and Banks 1987). They are repeated structures involving ridges of relatively small clasts with low degrees of cracking separated by depressions of coarser-grained breccia with high degrees of cracking. Our ridges have wavelengths of 10 m and amplitudes of 1 m. They are found towards the flow front and form down-flow of the raft zones. We interpret them as being ogives (Cas and Wright 1988) associated with folding due to piling up of lava behind a static or slowly moving flow front (Gregg et al. 1998). They are thus associated with zones where forward motion of the flow front has ceased, or has significantly decreased, but where flow has continued to be supplied into the back of the distal section of the system so as to cause deformation.

Quantitative analysis of surface folds

Surface folds can be characterized using high spatial resolution DEMs either as linear transects along the flow axis or by generating spectrograms via Fourier analysis (Lescinsky et al. 2007; Cashman et al. 2013). Fourier transforms of vertical profiles can be used to determine the frequencies (and wavelength λ) of sinusoidal patterns present in the data. However, conventional Fourier transforms are not able to determine the location along the profile of the component sinusoids, but instead give an "average spectrum for the entire data set" (Lescinsky et al. 2007). The *S*-transform method allows local spectral analysis to provide local values of amplitude and phase of sinusoidal spatial components, allowing local structure and patterns to be identified. The spatial component of the *S*-transform is obtained by multiplying the spatial data with a moving Gaussian window and by determining the Fourier transform for every point (Stokwell et al. 1996; Lescinsky et al. 2007). The Fourier transform is given by

$$F(k) = \int_{-\infty}^{+\infty} f(x) e^{-2\pi x k} dx$$

where k represents frequency, x is the distance, $f(x)$ is a given data series, and $F(k)$ is the Fourier transform. The one-dimensional *S*-transform is given by

$$S(k,u) = \int_{-\infty}^{+\infty} f(x) \left\{ \frac{|k|}{\sqrt{2\pi}} e^{-\left[(u-x)^2 k^2\right]/2} \right\} e^{-2\pi x k} dx$$

where u is the location within the profile and $S(k,u)$ corresponds to the calculated *S*-spectrum coefficients. The term within the curly brackets is the local Gaussian window at x. Additional details on the derivation and use of the *S*-transform are described by Stockwell et al. (1996) and Lescinsky et al. (2007).

Because the range of λ resolvable by the Fourier and *S*-transform approach is a function of the spatial resolution of the data, as well as of the length of the data profile, we compare the spectral analysis of two selected vertical profiles extracted from SfM and LiDAR data. *S*-spectrum plots of two selected topographic profiles (Figs. 9 and 10) reveal the presence of horizontal bands and patches of high coherence values. Significant features are identified as those that have higher coherence than surrounding values of similar wavelength, and which correspond to sinusoidal structures (Lescinsky et al. 2007). Synthetic sinusoids of appropriate λ and amplitude are provided for visualization in the profiles of Figs. 9 and 10. *S*-spectrum plots of topographic profiles in the 20-cm data reveal numerous horizontal bands and patches of high coherence values that are absent in the 1-m topographic profiles. *S*-spectrum plots of the Fig. 9 transect reveal, for the 1-m DEM, only one feature with $\lambda =$ 8.0 m. The same transect taken down the 20-cm DEM reveals two bands with different wavelengths ($\lambda = 4.6$ and $\lambda =$ 3.3 m), neglecting the bands at the edge of the transect. These overlap at points along the profile, indicating a superposition of multiple structures and implying multiple formation events (Fink and Fletcher 1978). Figure 10 gives the *S*-spectrum of a different profile over the 1974 lava flow. In this case, in the 20-cm *S*-spectrum plot, we find as many as three discrete formation events, with λ values for these features of 2.6, 4.4, and 5.8 m. Conversely, in the 1-m *S*-spectrum, only one feature, with $\lambda = 4.7$, is identifiable (Fig. 10).

Lava flow morphometric analysis

The high spatial resolution topography of Etna's 1974 lava flow was also used to extract morphometric parameters for three different channel-fed lava flows: a mature channel (Fig. 11), an immature channel with low yield strength (Fig. 12), and an immature channel with high yield strength (Fig. 13). These profiles allow quantitative description of the lava flow morphology using flow width (W_f), levee width (W_l), channel width (W_c), downstream local slope angle of the levees (θ_l), and the slope of the channel axis (θ) (for definition of each parameter, see Fig. 11). Each of these parameters is recorded as a function of distance down the flow centerline from the vent to the flow front.

Figures 11, 12, and 13 plot the evolution of morphology down the flow centerline for each case. The mature channel case of Fig. 11 is a ~500-m-long channel characterized by well-formed levees, except where filled by undrained lava from the final pulse that moved down the upper portion of the channel (Fig. 11b). Near-vent, the channel undergoes only

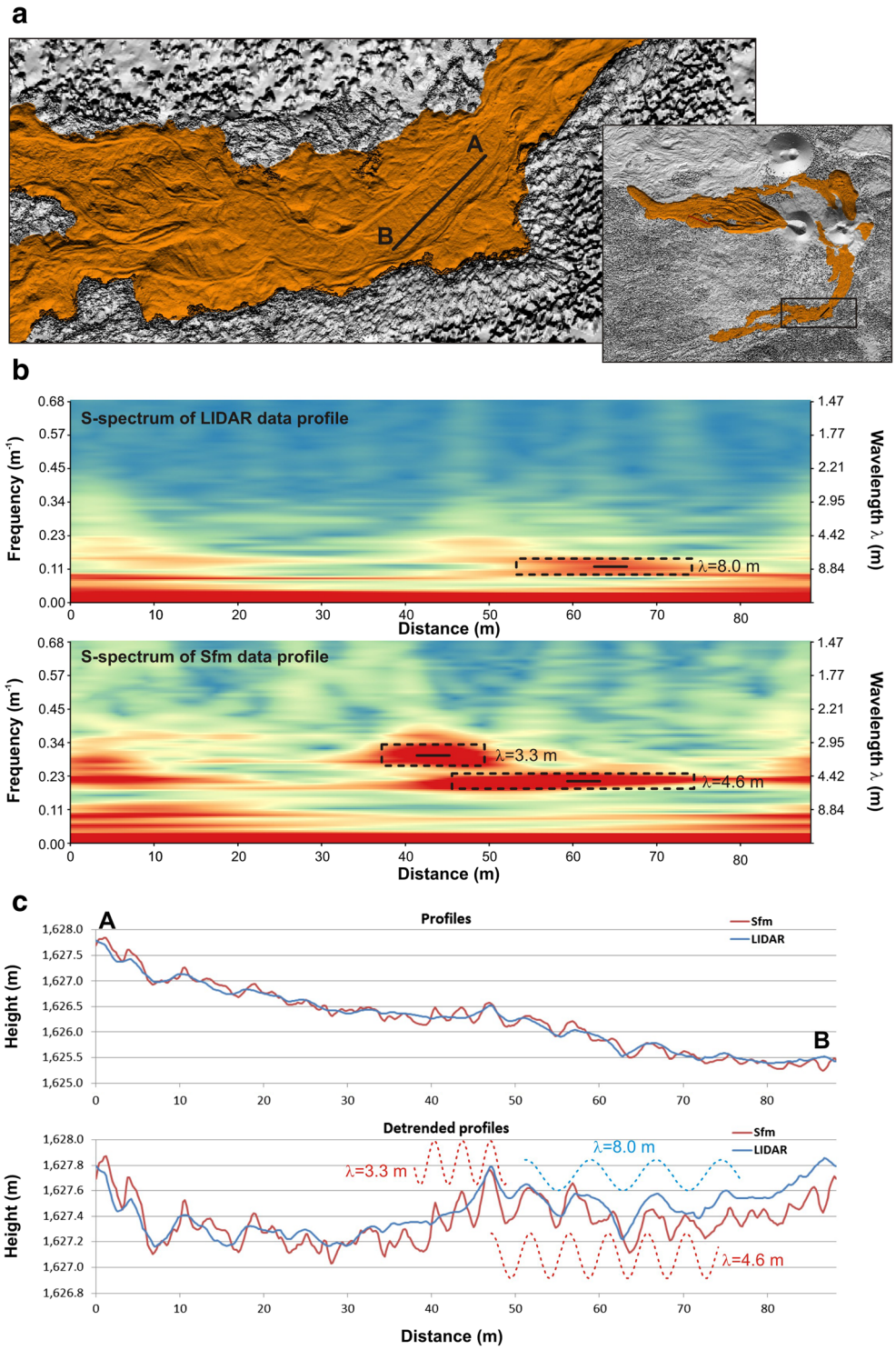

Fig. 9 **a** Location of profile taken down the center of the master channel feeding the longest lava flow field emplaced during phase 1 of Etna's January–February 1974 eruption. Inset is the flow field location map on which the enlargement is located (1974 lavas are in orange on the shaded relief from the merged of the LiDAR-DEM and SfM-DEM). **b** *S*-spectrum of the profile from the LiDAR and SfM-DEM, respectively. Red and yellow colors correspond to high coherence, and blue to low coherence. Dashed black boxes highlight zones of high coherence; black lines correspond to specific wavelengths plotted in **c**. **c** Topographic profile (top) and detrended profiles of the mean slope (below). Dashed lines indicate synthetic sinusoids with their characteristic wavelengths and amplitudes

a very slight decrease in width, decreasing in width by 10 m over the first 350 m. After reaching this minima, the channel then increases in width until the zone of dispersed flow, at which point the width reaches a maximum of 40 m. Beyond this point, the 125-m-long zone of dispersed flow opens out to a maximum width of ~ 115 m near the flow front. Folds just behind the flow front are particularly well formed (Fig. 11b).

The low yield strength (immature) channel of Fig. 12 is ~ 1200 m long. The levees are continuous only for the first 500 m, down which W_l has the same value as the mature channel of Fig. 11 (i.e., about 30 m). Beyond this, the zone of dispersed flow is ~ 750 m long, with a much more complex surface morphology than the mature case, as revealed by openness down map (Fig. 12b, c).

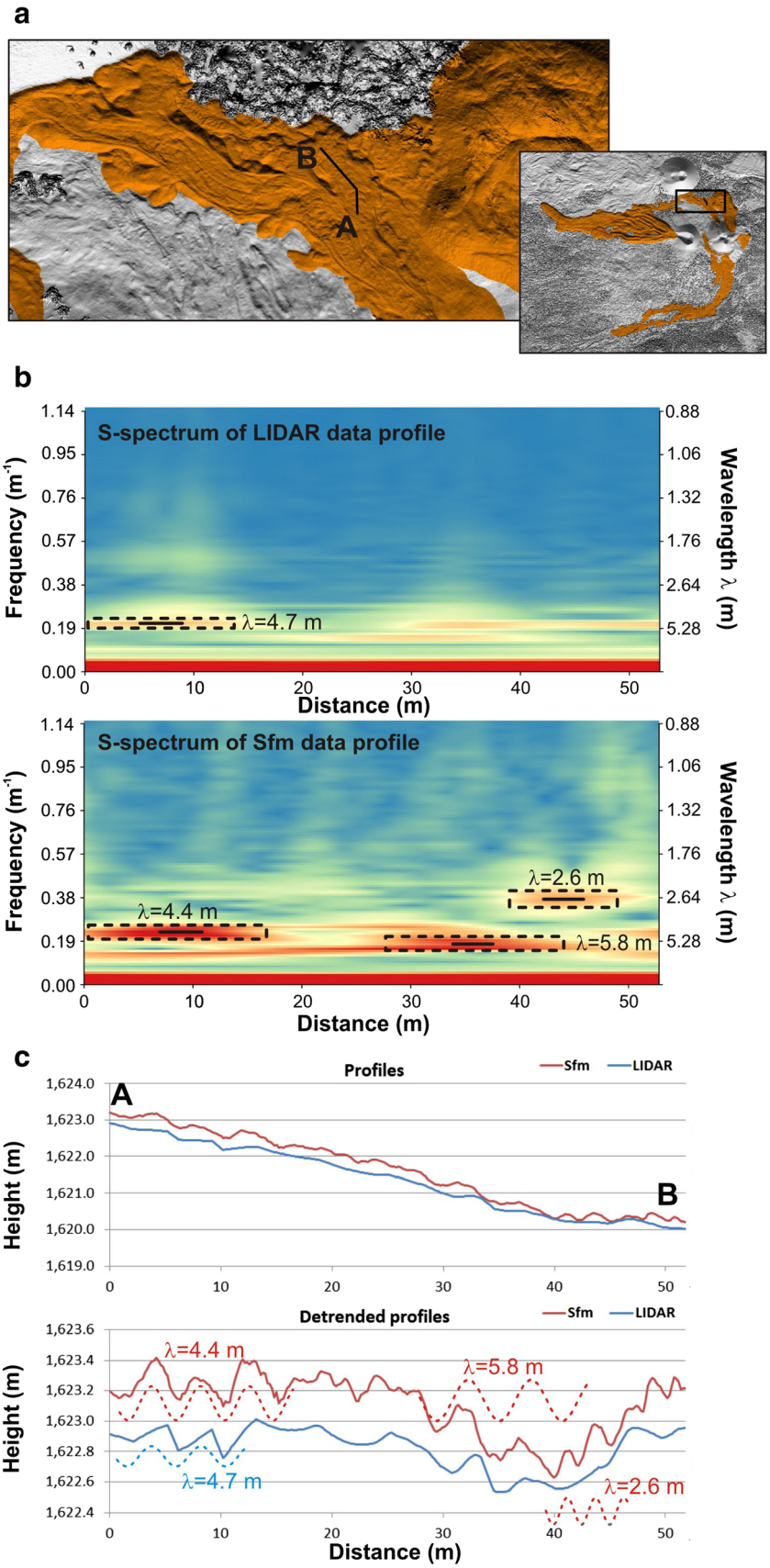

Fig. 10 **a** Location of profile taken down the center of channel feeding lava flow emplaced during phase 2 of Etna's January–February 1974 eruption. Inset is the flow field location map on which the enlargement is located (1974 lavas are in orange on the shaded relief from the merged of the LiDAR-DEM and SfM-DEM). **b** *S*-spectrum of the profile from the LiDAR and SfM-DEM, respectively. Red and yellow colors correspond to high coherence, and blue to low coherence. Dashed black boxes highlight zones of high coherence; black lines correspond to specific wavelengths plotted in **c**. **c** Topographic profile (top) and detrended profiles of the mean slope (below). Dashed lines indicate synthetic sinusoids with their characteristic wavelengths and amplitudes

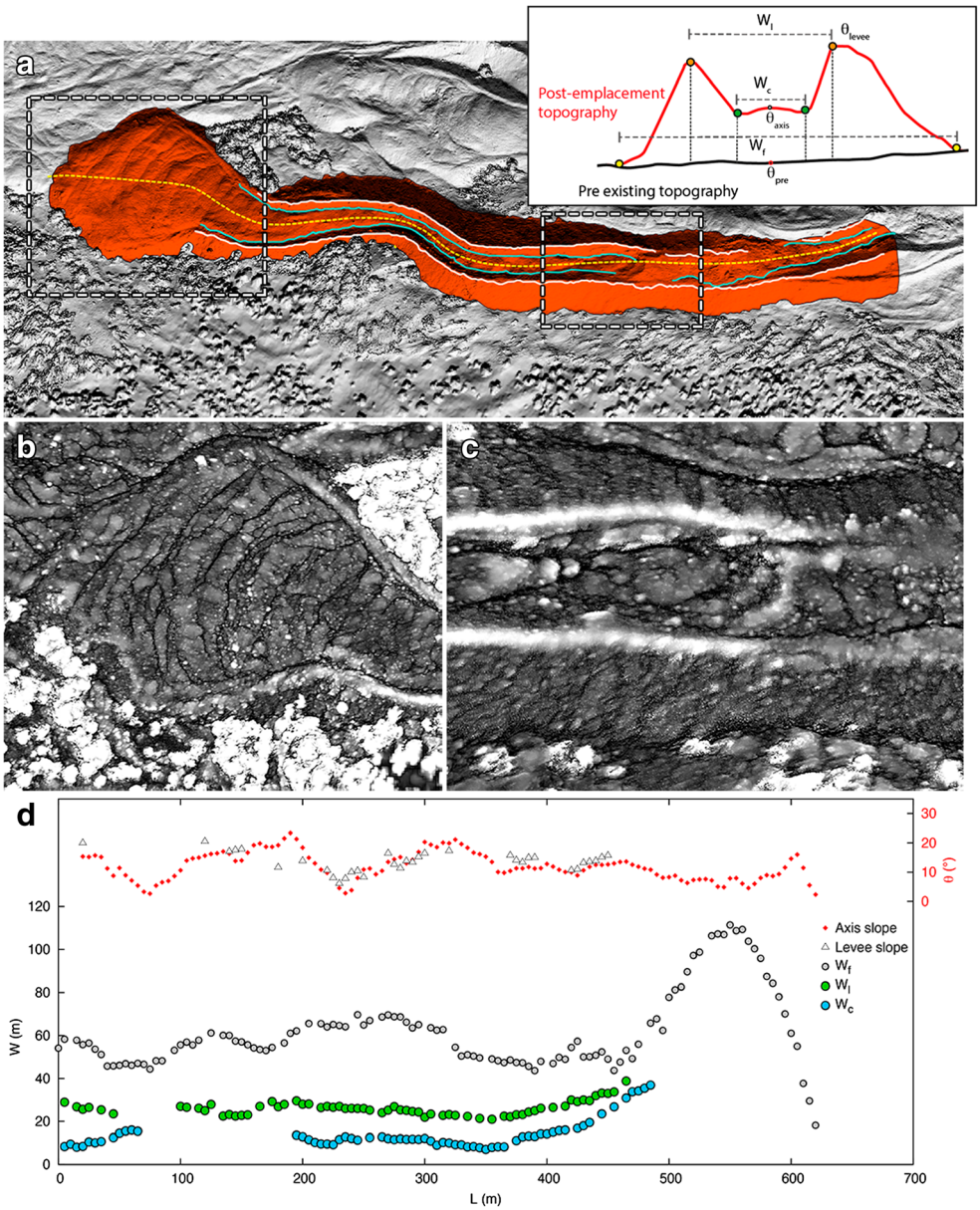

Fig. 11 Morphometric analysis of a mature channel. The channel system is filled with orange in **a**. **a** Channel axis is given by the yellow line, and levee rims by the white lines, and magnifications are located by dashed-line boxes. **b** Openness down (crack) map of the zone of dispersed flow. **c** Openness down (crack) map of the stable channel. **d** Down system profiles of flow width (W_f), levee width (W_l), and channel width (W_c), plus the local slope angle of the levees and the slope of the channel axis (schematic showing measurement system is given as inset in **a**)

The high-yield-strength (immature) channel of Fig. 13 has a well-defined shape and is 450 m long. It is characterized by a wide channel, with a maximum W_l value of ~125 m in the distal zone. Morphological structures are well developed in the proximal reach of the channel (Fig. 13c), and are complex in the zone of dispersed flow (Fig. 13b).

Summarizing the results of this morphological analysis, Figs. 11, 12, and 13 show that local variations in the slope angle are sufficient to significantly scatter the data and that θ is correlated with θ_l. The plots show also that the downhill increase in channel width found by Mazzarini et al. (2005) and Tarquini et al. (2012) is not a general rule for Etna channels, with W_l of Figs. 11 and 12 having different trends for different segments. While a negative correlation between θ and channel width is present for the channel of Fig. 13, W_f and W_c have almost the same down-flow trend in all cases.

Such morphometric parameters are much needed as benchmark controls or validation, as well as initial or boundary conditions, for lava flow modeling (Harris et al. 2007; Tarquini et al. 2012; Lev and James 2014; Cordonnier et al. 2016). They are, though, lacking in quantity and accuracy. The importance of accurate morphometric measurements was also stressed by Chevrel et al. (2013), who showed that the propagation of even small errors in channel measurements can cause a large spread in derived rheological properties.

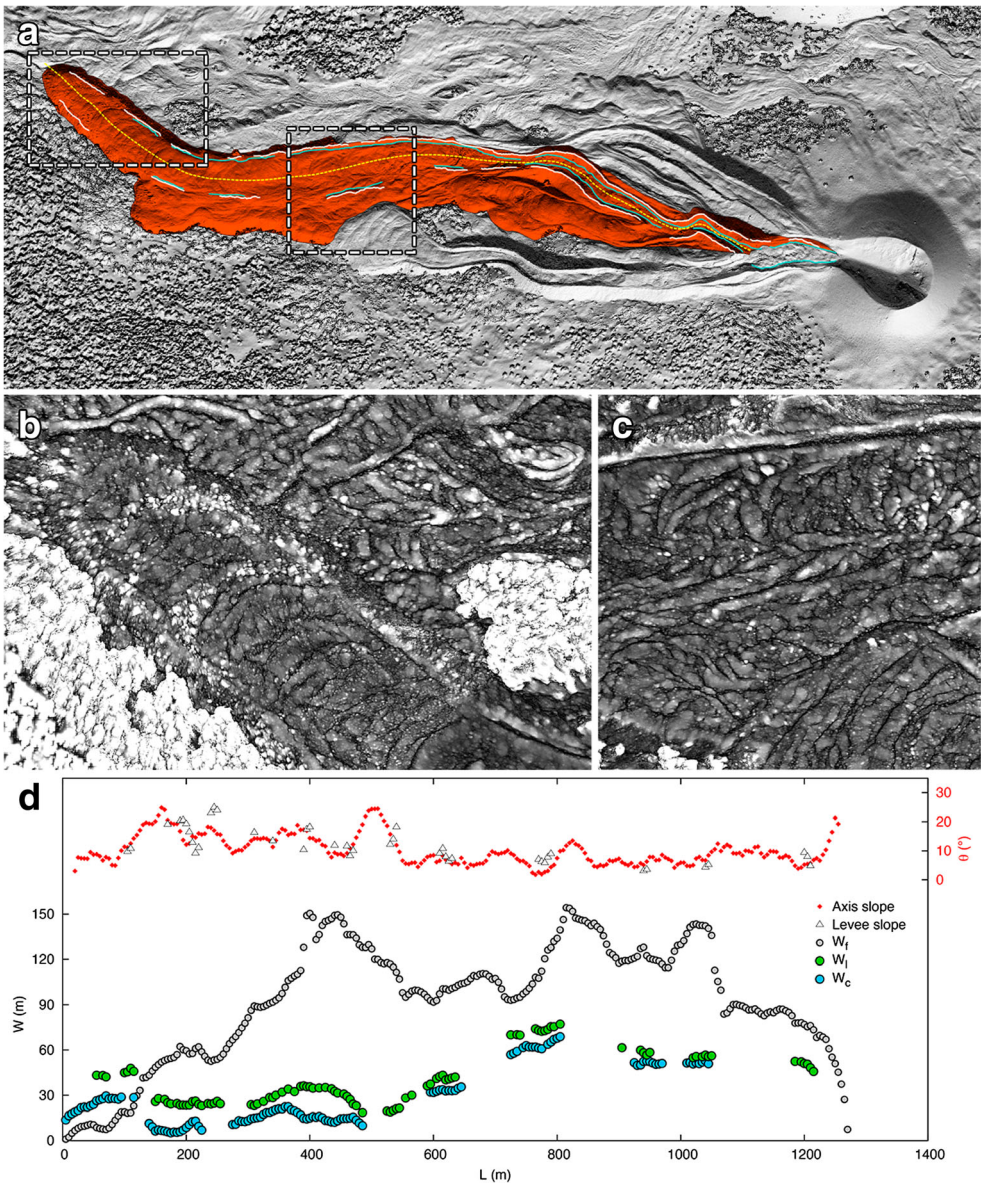

Fig. 12 Morphometric analysis of an immature channel with low yield strength. The channel system is filled with orange in **a**. **a** Channel axis is given by the yellow line, and levee rims by the white lines, and magnifications are located by dashed-line boxes. **b** Openness down (crack) map of the zone of dispersed flow. **c** Openness down (crack) map of the stable channel. **d** Down system profiles of flow width (W_f), levee width (W_l), and channel width (W_c), plus the local slope angle of the levees and the slope of the channel axis (schematic showing measurement system is given as inset in Fig. 11a)

Hazard assessment implications

During an effusive eruption, it is of paramount importance to map, in as precise and timely manner as possible, the location and direction of newly forming lava flows and their distribution systems. This is normally carried out through helicopter surveys, supported by airborne thermal camera operations or through satellite mapping (e.g., Harris et al. 2005; Spampinato et al. 2011; Ganci et al. 2012a, b; Harris 2013). However, ash emission from explosive activity at nearby eruptive fissures, or from smoke from forests burning at the lava flow front, can impede or even ground traditional airborne surveys (e.g., Patrick et al. 2017; Turner et al. 2017), as during Etna's 2002–2003 eruption (Andronico et al. 2005; Bonaccorso et al. 2016). Under such conditions, the use of UAV to obtain timely and extremely high spatial resolution data of a developing lava flow field is an extremely attractive option. UAVs have already been successfully used during an ongoing eruption as described by Perroy et al. (2015). Although surveys near active vents are reasonably problematic, data collection along an active lava flow is possible if a proper flight path has been planned before of UAV take off. Our work demonstrates that a large area, which includes the zone of dispersed flow, can be mapped using the UAV-SfM method every 1–2 h, which can be considered a near-real-time acquisition given the relatively slow advance of a lava flow front. The resulting output allows immediate analysis of flow morphology and structure, as well as analysis of changes in flow geometry over short time scales. Reporting based on such data allows a scientist-in-charge at an active site to advise civil protection authorities, and then populations at risk, regarding the hazard to which they are exposed, and to provide updates

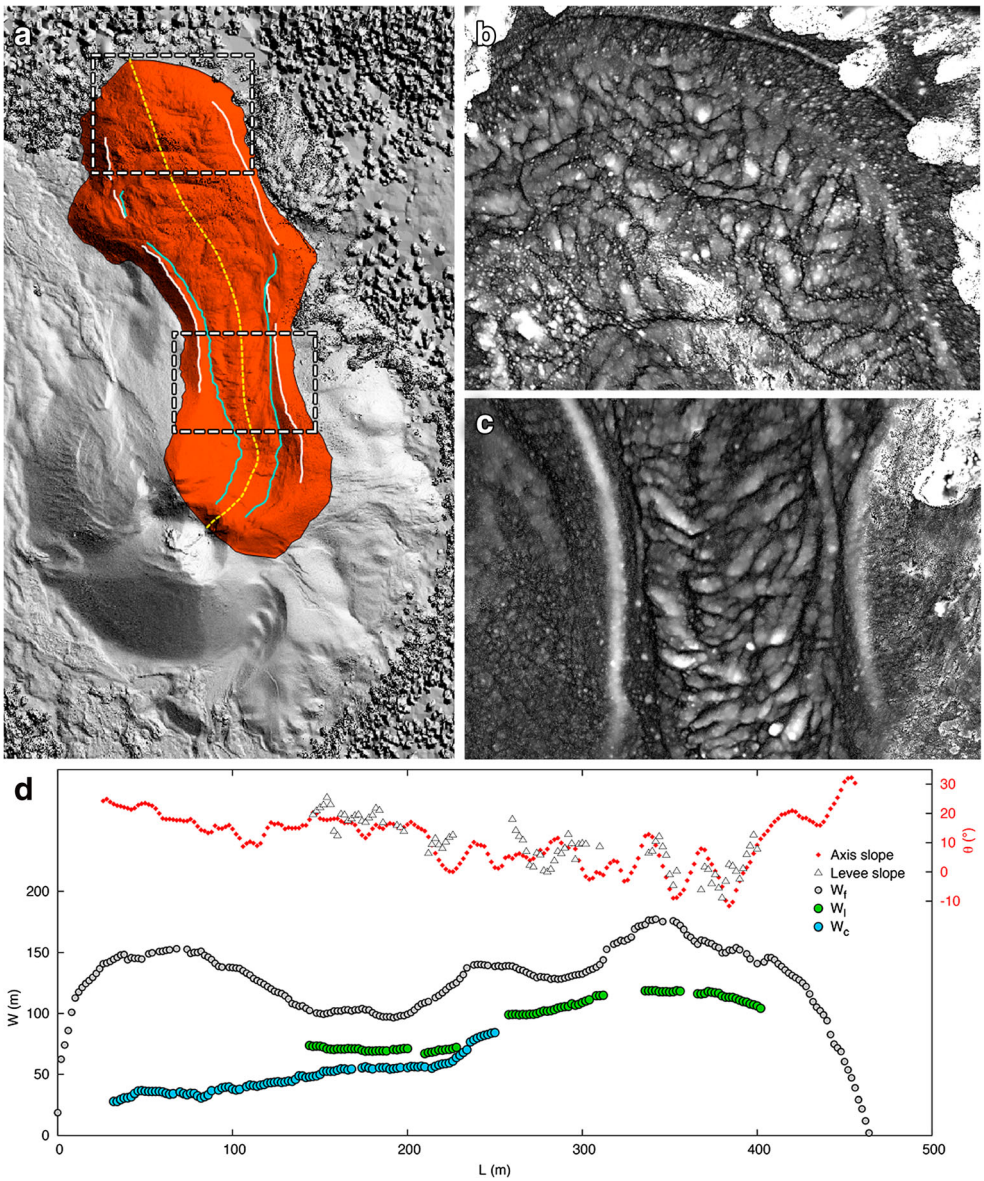

Fig. 13 Morphometric analysis of an immature channel with high yield strength. The channel system is filled with orange in **a**. **a** Channel axis is given by the yellow line, and levee rims by the white lines, and magnifications are located by dashed-line boxes. **b** Openness down (crack) map of the zone of dispersed flow. **c** Openness down (crack) map of the stable channel. **d** Down system profiles of flow width (W_f), levee width (W_l), and channel width (W_c), plus the local slope angle of the levees and the slope of the channel axis (schematic showing measurement system is given as inset in Fig. 11a)

on a regular basis. In addition, the drone-based platform provides a low-cost, flexible option (in terms of deployment, as well as spatial and temporal resolution), which can be deployed as needed with low risk to those involved in implementing the observation tasks.

Take the following scenario. A SfM-UAV-derived DEM is obtained in which shear lines, similar to those observed in Fig. 7, are detected. Because such structures form when a sheet flow becomes channelized, this indicates the developing location of the main channel. Given that a channel focuses lava towards vulnerable populations more efficiently than sheet flow, this represents a concern. As a result, the development, orientation, dimensions and extension (with time) of such features need to be tracked. Thus, the evolution of the supply system then needs to be monitored through frequent surveys by drone so as to obtain continuously updated DEMs in which the changes in position, orientation and size of channels comprising the distribution system can be monitored. With time, a lava channel system will develop into a lava tube system (Peterson et al. 1994; Kauahikaua et al. 1998). This will now increase the risk to communities in the flow path, because increased insulation and lower cooling rates caused by formation of the tube roof (Keszthelyi 1995) will increase the potential for inundation of more distant communities to be inundated by lava. At this point, it becomes of paramount importance to map the distribution of breakouts and supply from ephemeral vents, because these will reveal the presence of well-fed lava tubes developing within the lava flow field (Calvari and Pinkerton 1998; Duncan et al. 2004) and their emission points.

DEMs obtained on an hourly-to-daily basis allow the formation of channels to be detected and followed, and the rate of expansion of lava coverage and mass eruption rate to be

calculated (James and Robson 2014a). The SfM-UAV very high spatial resolution DEM reconstruction performed in this work required some time to develop, an amount of time (several days) which would be incompatible with hazard management. However, now operational, if applied during a volcanic crisis the survey and methods here described could be sped up so as to decrease the processing time at the cost of a lower resolution DEM, as dictated by hazard evaluation and modeling needs. For example, a simple test performed with Photoscan on a sample of 100 photos using a normal desktop computer took three hours to generate the highest possible resolution 3D model comprising 200 million points. It then took less than five minutes to generate the lowest possible resolution model of about one million points.

Conclusions

For monitoring and surveillance of volcanic terrains, unmanned aerial vehicles (UAV), otherwise known as drones, are excellent platforms for acquiring high spatial resolution photogrammetric data with high temporal resolution. These data can then be used to map surface features that inform on lava flow emplacement dynamics. In our case, a UAV-mounted digital camera capability, coupled with SfM methods, allowed generation of a 20-cm resolution DEM for the 1974 Mount Etna lava flow field, enabling analysis of sub-meter-scale features over an area of several square kilometers. The 20-cm spatial resolution allowed morphometric analysis of lava surface features such as folds, blocks, and cracks in a manner not possible with the 1-m LiDAR-derived DEM. Merging these data with the 3-cm orthophoto allowed us to further push the analysis to allow centimeter-scale grain distribution of the lava surface, and spectral analysis of surface folding over a much larger spectrum of frequencies than was possible using the LiDAR-derived DEM. In this regard, geometry of surface folding can be used to constrain the thickness and viscosity of the folded layer (from the fold wavelength) and compressional stress (from the fold amplitude). At the same time, recognizing initial levee formation, generation of lava channels, and, eventually, lava tube formation aids in hazard tracking and assessment. This is just one example of how UAV-based 3D modeling can be used to measure and parameterize structural, rheological, and dynamic features in extensive, complex, and spatially variable compound lava flow fields.

UAVs allow surveys of inaccessible, kilometer-scale areas, with low cost and minimal hazard to personnel. This is a distinct advantage over a volcanic terrain where time scales of change are fast (minutes to hours), involve vertical spatial scales of millimeters to meters, and are extremely hazardous to approach. This is an argument that has been applied for several decades (e.g., see Harris 2013 for full review), but the advent of the UAV means that an operator can truly update the topography every few hours for an outlay of just a few thousand Euros (this being the price of the drone, the camera, and the autopilot software, in our case). Better, freely available, and easy-to-use SfM-based software allows update of a pre-existing DEM, or creation of a new DEM, in a timely fashion. Alongside this, the flexibility of the flight plan and frequency presented by the user-operated UAV platform, and the quality of off-the-shelf digital cameras, means filling of topographic data gaps is straightforward, and the horizontal and vertical resolutions of DEMs can be reduced to centimetric.

Acknowledgements The UAV was partially funded by the EU under the LIFE12/ENV/IT/001033 Wireless sensor network for the Ground Instability Monitoring (Wi-GIM) project. AF has carried out this work in the frame of his Doctorate in Geophysics at the Department of Physics and Astronomy, University of Bologna. The authors are grateful to the Editor, Michael R. James, and to Matt Patrick and Einat Lev for comments that greatly improved the clarity of our science and writing. Both the 20-cm SfM-UAV DEM and 20-cm orthomosaic derived here are provided as supplementary material.

References

Andronico D, Branca S, Calvari S, Burton M, Caltabiano T, Corsaro RA, Del Carlo P, Garfì G, Lodato L, Miraglia L, Muré F, Neri M, Pecora E, Pompilio M, Salerno G, Spampinato L (2005) A multi-disciplinary study of the 2002–03 Etna eruption: insights into a complex plumbing system. Bull Volcanol 67:314–330. https://doi.org/10.1007/s00445-004-0372-8

Behncke B, Fornaciai A, Neri M, Favalli M, Ganci G, Mazzarini F (2016) Lidar surveys reveal eruptive volumes and rates at Etna, 2007–2010. Geophys Res Lett 43(9):4270–4278. https://doi.org/10.1002/2016GL068495

Bonaccorso A, Calvari S, Boschi E (2016) Hazard mitigation and crisis management during major flank eruptions at Etna volcano: reporting on real experience. In: Harris AJL, De Groeve T, Garel F, Carn SA (eds) Detecting, modelling and responding to effusive eruptions. Geological Society London, Special Publications (IAVCEI) Series 426. https://doi.org/10.1144/SP426.4

Bottari A, Lo Giudice E, Patanè G, Romano R, Sturiale C (1975) L'eruzione etnea del gennaio-marzo 1974. Rivista Mineralogica Siciliana 154(156):175–198

Calvari S, Pinkerton H (1998) Formation of lava tubes and extensive flow field during the 1991-93 eruption of Mount Etna. J Geophys Res 103(B11):27291–27302

Cas RAF, Wright JV (1988) Lava flows in volcanic successions modern and ancient, vol 4. Springer, Netherlands, pp 58–91

Cashman KV, Soule SA, Mackey BH, Deligne NI, Deardorff ND, Dietterich HR (2013) How lava flows: new insights from applications of lidar technologies to lava flow studies. Geosphere 9(6):1664–1680

Chevrel MO, Platz T, Hauber E, Baratoux D, Lavallée Y, Dingwell DB (2013) Lava flow rheology: a comparison of morphological and petrological methods. Earth Planet Sci Lett 384:109–120

Cordonnier B, Lev E, Garel F (2016) Benchmarking lava-flow models. Geol Soc Lond, Spec Publ 426(1):425–445

Corsaro RA, Métrich N, Allard P, Andronico D, Miraglia L, Fourmentraux C (2009) The 1974 flank eruption of Mount Etna: an archetype for deep dike-fed eruptions at basaltic volcanoes and a milestone in Etna's recent history. J Geophys Res 114(B7): B07204. https://doi.org/10.1029/2008JB006013

Crown DA, Baloga SM (1999) Pahoehoe toe dimensions, morphology, and branching relationships at Mauna Ulu, Kilauea Volcano, Hawai'i. Bull Volcanol 61(5):288–305

Deardorff ND, Cashman KV (2012) Emplacement conditions of the c. 1, 600-year BP Collier Cone lava flow, Oregon: a LiDAR investigation. Bull Volcanol 74(9):2051–2066

Dietterich HR, Cashman KV (2014) Channel networks within lava flows: formation, evolution, and implications for flow behavior. J Geophys Res 119(8):1704–1724. https://doi.org/10.1002/2014JF003103

Dietterich HR, Soule SA, Cashman KV, Mackey BH (2015) Lava flows in 3D. In: Carey R, Cayol V, Poland M, Weis D (eds) Hawaiian volcanoes: from source to surface. John Wiley & Sons Inc, Hoboken. https://doi.org/10.1002/9781118872079.ch22

Duncan AM, Guest JE, Stofan ER, Anderson SW, Pinkerton H, Calvari S (2004) Development of tumuli in the medial portion of the 1983 aa flow-field, Mount Etna, Sicily. J Volcanol Geotherm Res 132:173–187

Farquharson JI, James MR, Tuffen H (2015) Examining rhyolite lava flow dynamics through photo-based 3D reconstructions of the 2011–2012 lava flowfield at Cordón-Caulle, Chile. J Volcanol Geotherm Res 304:336–348

Favalli M, Fornaciai A (2017) Visualization and comparison of DEM-derived parameters. Application to volcanic areas. Geomorphology 290:69–84

Favalli M, Fornaciai A, Pareschi MT (2009) LIDAR strip adjustment: application to volcanic areas. Geomorphology 111(3):123–135. https://doi.org/10.1016/j.geomorph.2009.04.010

Favalli M, Fornaciai A, Mazzarini F, Harris A, Neri M, Behncke B, Pareschi MT, Tarquini S, Boschi E (2010a) Evolution of an active lava flow field using a multitemporal LIDAR acquisition. J Geophys Res Solid Earth 115(B11):B11203. https://doi.org/10.1029/2010JB007463

Favalli M, Harris AJ, Fornaciai A, Pareschi MT, Mazzarini F (2010b) The distal segment of Etna's 2001 basaltic lava flow. Bull Volcanol 72(1):119–127. https://doi.org/10.1007/s00445-009-0300-z

Favalli M, Fornaciai A, Isola I, Tarquini S, Nannipieri L (2012) Multiview 3D reconstruction in geosciences. Comput Geosci 44: 168–176

Fink J (1980) Surface folding and viscosity of rhyolite flows. Geology 8(5):250–254

Fink JH, Fletcher RC (1978) Ropy pahoehoe: surface folding of a viscous fluid. J Volcanol Geotherm Res 4(1):151–170

Fornaciai A, Bisson M, Landi P, Mazzarini F, Pareschi MT (2010) A LiDAR survey of Stromboli Volcano (Italy): digital elevation model-based geomorphology and intensity analysis. Int J Remote Sens 31(12):3177–3194

Fornaciai A, Favalli M, Nannipieri L, Harris A, Calvari S, Lormand C (2017) High-resolution topography of 1974 Mount Etna lava flow based on unmanned aerial vehicle (UAV) surveys and structure from motion (SfM) photogrammetry. EGU General Assembly Conference Abstracts 19 15337

Francis P, Rothery D (2000) Remote sensing of active volcanoes. Annu Rev Earth Planet Sci 28(1):81–81

Ganci G, Vicari A, Cappello A, Del Negro C (2012a) An emergent strategy for volcano hazard assessment: from thermal satellite monitoring to lava flow modeling. Remote Sens Environ 119:197–207

Ganci G, Harris AJL, Del Negro C, Guehenneux Y, Cappello A, Labazuy P, Calvari S, Gouhier M (2012b) A year of lava fountaining at Etna: volumes from SEVIRI. Geophys Res Lett 39:L06305. https://doi.org/10.1029/2012GL051026

Gregg TK, Fink JH (2000) A laboratory investigation into the effects of slope on lava flow morphology. J Volcanol Geotherm Res 96(3): 145–159

Gregg TK, Fink JH, Griffiths RW (1998) Formation of multiple fold generations on lava flow surfaces: influence of strain rate, cooling rate, and lava composition. J Volcanol Geotherm Res 80(3):281–292

Guest JE, Stofan ER (2005) The significance of slab-crusted lava flows for understanding controls on flow emplacement at Mount Etna, Sicily. J Volcanol Geotherm Res 142(3):193–205

Harris A (2013) Thermal remote sensing of active volcanoes: a user's manual. Cambridge University Press, Cambridge 728 p

Harris A, Dehn J, Patrick M, Calvari S, Ripepe M, Lodato L (2005) Lava effusion rates from hand-held thermal infrared imagery: an example from the June 2003 effusive activity at Stromboli. Bull Volcanol 68: 107–117

Harris A, Favalli M, Mazzarini F, Pareschi MT (2007) Best-fit results from application of a thermo-rheological model for channelized lava flow to high spatial resolution morphological data. Geophys Res Lett 34(1):L01301. https://doi.org/10.1029/2006GL028126

Harris AJ, Favalli M, Mazzarini F, Hamilton CW (2009) Construction dynamics of a lava channel. Bull Volcanol 71(4):459–474

James MR, Robson S (2012) Straightforward reconstruction of 3D surfaces and topography with a camera: accuracy and geoscience application. J Geophys Res Earth Surf 117(F3):F03017. https://doi.org/10.1029/2011JF002289

James MR, Robson S (2014a) Sequential digital elevation models of active lava flows from ground-based stereo time-lapse imagery. ISPRS J Photogramm Remote Sens 97:160–170

James MR, Robson S (2014b) Mitigating systematic error in topographic models derived from UAV and ground-based image networks. Earth Surf Process Landf 39:1413–1420. https://doi.org/10.1002/esp.3609

James F, Roos M, (1977) MINUIT, CERN Program Library Entry D506

James MR, Varley N (2012) Identification of structural controls in an active lava dome with high resolution DEMs: Volcán de Colima, Mexico. Geophys Res Lett 39(22):L22303. https://doi.org/10.1029/2012GL054245

James MR, Pinkerton H, Applegarth LJ (2009) Detecting the development of active lava flow fields with a very-long-range terrestrial laser scanner and thermal imagery. Geophys Res Lett 36(22): L22305. https://doi.org/10.1029/2009GL040701

Karátson D, Yepes J, Favalli M, Rodríguez-Peces MJ, Fornaciai A (2016) Reconstructing eroded paleovolcanoes on Gran Canaria, Canary Islands, using advanced geomorphometry. Geomorphology 253: 123–134

Kauahikaua J, Cashman KV, Mattox TN, Heliker CC, Hon KA, Mangan MT, Thornber CR (1998) Observations on basaltic lava streams in tubes from Kilauea Volcano, island of Hawai'i. J Geophys Res 103(B11):27303–27323. https://doi.org/10.1029/97JB03576

Keszthelyi L (1995) A preliminary thermal budget for lava tubes on the Earth and planets. J Geophys Res Solid Earth 100(B10):20411–20420

Kolzenburg S, Favalli M, Fornaciai A, Isola I, Harris AJL, Nannipieri L, Giordano D (2016) Rapid updating and improvement of airborne LIDAR DEMs through ground-based SfM 3-D modeling of volcanic features. IEEE Trans Geosci Remote Sens 54(11):6687–6699

Lescinsky DT, Merle O (2005) Extensional and compressional strain in lava flows and the formation of fractures in surface crust. Geol Soc Am Spec Pap 396:163–179. https://doi.org/10.1130/0-8137-2396-5

Lescinsky DT, Skoblenick SV, Mansinha L (2007) Automated identification of lava flow structures using local Fourier spectrum of digital elevation data. J Geophys Res 112(B5):B05212. https://doi.org/10.1029/2006JB004263

Lev E, James MR (2014) The influence of cross-sectional channel geometry on rheology and flux estimates for active lava flows. Bull Volcanol 76(7):1–15

Lillesand TM, Kiefer RW, Chipman JW (1987). Remote sensing and image interpretation. John Wiley & Sons, New York.

Lipman PW, Banks NG (1987) Aa flow dynamics, Mauna Loa 1984. Volcanism in Hawaii. RW Decker, TL Wright and PH Stauffer. Washington, USGS Professional Paper 1350:1527-1567

Lucieer A, Jong SMD, Turner D (2014) Mapping landslide displacements using structure from motion (SfM) and image correlation of multi-temporal UAV photography. Prog Phys Geogr 38(1):97–116

Mancini F, Dubbini M, Gattelli M, Stecchi F, Fabbri S, Gabbianelli G (2013) Using unmanned aerial vehicles (UAV) for high-resolution reconstruction of topography: the structure from motion approach on coastal environments. Remote Sens 5(12):6880–6898

Mazzarini F, Pareschi MT, Favalli M, Isola I, Tarquini S, Boschi E (2005) Morphology of basaltic lava channels during the Mt. Etna September 2004 eruption from airborne laser altimeter data. Geophys Res Lett 32(4):L04305. https://doi.org/10.1029/2004GL021815

Müller D, Walter TR, Schöpa A, Witt T, Steinke B, Gudmundsson MT, Dürig T (2017) High-resolution digital elevation modeling from TLS and UAV campaign reveals structural complexity at the 2014/2015 Holuhraun eruption site, Iceland. Front Earth Sci 5:59. https://doi.org/10.3389/feart.2017.00059

Nakano T, Kamiya I, Tobita M, Iwahashi J, Nakajima H (2014) Landform monitoring in active volcano by UAV and SfM-MVS technique. Int Arc Photogramm Remote Sens Spat Inf Sci 40(8):71–75

Nannipieri L, Fornaciai A, Favalli M, Cipolla V (2016) Manuale delle operazioni con SAPR e analisi del rischio. Rapporti Tecnici INGV 346 ISSN 2039-7941. http://www.ingv.it/editoria/rapporti/2016/rapporto346/

Neri M, De Maio M, Crepaldi S, Suozzi E, Lavy M, Marchionatti F, Calvari S, Buongiorno MF (2017) Topographic maps of Mount Etna's summit craters, updated to December 2015. J Maps 13(2):674–683

Nouwakpo SK, Weltz MA, McGwire K (2016) Assessing the performance of structure-from-motion photogrammetry and terrestrial LiDAR for reconstructing soil surface microtopography of naturally vegetated plots. Earth Surf Process Landf 41(3):308–322

Patrick MR, Orr T, Fisher G, Trusdell F, Kauahikaua J (2017) Thermal mapping of a pahoehoe lava flow, Kilauea Volcano. J Volcanol Geotherm Res 332:71–87. https://doi.org/10.1016/j.jvolgeores.2016.12.007

Perroy R, Turner N, Hon K, Rasgado V (2015) Monitoring inflation and emplacement during the 2014-2015 Kīlauea lava flow with an unmanned aerial vehicle. American Geophysical Union Fall Meeting, Abstract V13D-03

Peterson DW, Holcomb RT, Tilling RI, Christiansen RL (1994) Development of lava tubes in the light of observations at Mauna Ulu, Kilauea Volcano, Hawaii. Bull Volcanol 56(5):343–360

Photoscan A (2013) Agisoft PhotoScan user manual professional edition. Agisoft LLC, St. Petersburg

Richter N, Favalli M, de Zeeuw-van Dalfsen E, Fornaciai A, da Silva Fernandes RM, Rodriguez NP, Levy J, Victória SS, Walter TR (2016) Lava flow hazard at Fogo Volcano, Cape Verde, before and after the 2014–2015 eruption. Nat Hazards Earth Syst Sci Discuss 16:1925–1951. https://doi.org/10.5194/nhess-2016-81

Rossi MJ (1997) Morphology of the 1984 open-channel lava flow at Krafla volcano, northern Iceland. Geomorphology 20:95–112

Slatcher N, James MR, Calvari S, Ganci G, Browning J (2015) Quantifying effusion rates at active volcanoes through integrated time-lapse laser scanning and photography. Remote Sens 7:14967–14987. https://doi.org/10.3390/rs71114967

Spampinato L, Calvari S, Oppenheimer C, Boschi E (2011) Volcano surveillance using infrared cameras. Earth Sci Rev 106:63–91

Stevens NF, Wadge G, Murray JB (1999) Lava flow volume and morphology from digitised contour maps: a case study at Mount Etna, Sicily. Geomorphology 28(3):251–261

Stockwell RG, Mansinha L, Lowe RP (1996) Localization of the complex spectrum: the S transform. IEEE Trans Signal Process 44(4):998–1001

Tanguy JC, Kieffer G (1977) The 1974 eruption of Mount Etna. Bull Volcanol 40(4):239–252

Tarquini S, Favalli M, Mazzarini F, Isola I, Fornaciai A (2012) Morphometric analysis of lava flow units: case study over LIDAR-derived topography at Mount Etna, Italy. J Volcanol Geotherm Res 235:11–22

Tuffen H, James MR, Castro JM, Schipper CI (2013) Exceptional mobility of a rhyolitic obsidian flow: observations from Cordón Caulle, Chile, 2011–2013. Nat Commun 2709

Turner NR, Perroy RL, Hon K (2017) Lava flow hazard prediction and monitoring with UAS: a case study from the 2014–2015 Pāhoa lava flow crisis, Hawaii. J Appl Volcanol 6(1):17

Westoby MJ, Brasington J, Glasser NF, Hambrey MJ, Reynolds JM (2012) 'Structure-from-Motion' photogrammetry: a low-cost, effective tool for geoscience applications. Geomorphology 179:300–314

Yokoyama R, Shirasawa M, Pike RJ (2002) Visualizing topography by openness: a new application of image processing to digital elevation models. Photogramm Eng Remote Sens 68(3):257–266

Zakšek K, Oštir K, Kokalj Ž (2011) Sky-view factor as a relief visualization technique. Remote Sens 3(2):398–415